Count-Rate Dependent Component-Based Normalization for the HRRT

Mario Rodriguez, Jeih-San Liow, *Member, IEEE*, Shanthalaxmi Thada, Merence Sibomana, Sudhakar Chelikani, *Member, IEEE*, Tim Mulnix, Calvin A. Johnson, Christian Michel, W. Craig Barker, and Richard E. Carson, *Member, IEEE*

***Abstract*—Component-based normalization is an important technique for PET scanners with a high number of lines of response (LOR), e.g., 4.5×10^9 for the HRRT. It reduces the problem of measuring the sensitivity of each LOR to that of estimating the individual crystal efficiencies (ε), e.g., 119808 for the HRRT. We propose a component-based method to compute ε for the HRRT. In addition, the block design of the HRRT produces pulse pile-up which causes apparent changes in ε with count rate. These effects occur within the block and between the front (LSO) and back (LYSO) crystal layers. We use a rotating source to measure the ε values and a decaying uniform phantom to account for ε variations with count rate. The computation of efficiencies is achieved with $\sim$1% statistical noise with an acquisition of $\sim$1 h. Count rate dependency of ε is implemented as a linear model in terms of block singles rate. Four approaches to modify ε with count rate were compared. Among them, an independent parameter for each crystal produced the best results, both visually and quantitatively. Failure to account for the count rate dependency in ε leads to high resolution artifacts in the reconstructed images, most visible in the transverse plane, in the center of the field-of-view.**

***Index Terms*—Component-based normalization, HRRT, MOLAR, pile-up effect.**

I. Introduction

RELIABLE image reconstruction in Positron Emission Tomography (PET) cannot be achieved without correcting for the efficiency differences of lines of response (LOR) to detect pairs of annihilation photons. Direct normalization techniques, where the efficiencies are measured independently for each LOR, are the most obvious approach to achieve this correction [1]. The development of high resolution and three dimensional scanners produced systems with large numbers of LORs. In this case, methods to extend normalization factors from 2D to 3D have been developed [2]. However, direct normalization techniques have drawbacks in fully 3D scanners, i.e., in order to achieve high statistical accuracy of the normalization factors, either very long acquisitions or high activity sources (with randoms and deadtime effects) are required [3]. Component-based normalization (CBN) [4]–[8] methods provide an approach to determine normalization coefficients with high statistics and relatively short durations of data acquisition. CBN techniques are based on decomposing each LOR normalization factor into its components so that a much smaller number of parameters must be determined. For example, the minimum number of parameters is the number of crystals, in which case the parameters are the individual crystal efficiencies which are used to compute the normalization coefficient for each LOR.

Usually, the components that are included in the normalization model describe detector intrinsic properties, detection geometry and effects derived from detector design. Among the last category, the block detector design introduces an important effect that should ideally be included in the normalization, i.e., pulse pile-up [9]. In general, pulse pile-up occurs at high counting rates and tends to misposition events from the edges of the block towards the center. Pile-up causes several factors in the normalization model to become count rate dependent [6] and quantification and resolution degradations result if this effect is ignored. Several hardware-based techniques have been developed and implemented in order to minimize the effects caused by pile-up [10]–[12]. These methods attempted to recover the correct position of photon interaction through modifications in the electronics that process the detector signal. One proposed software-based approach includes a dead time correction technique that depends on the detector position within the block [4]. Alternatively, it has been proposed to obtain a series of normalization acquisitions at different count rates in order to correct for the count rate dependency of normalization factors using a look up table [6]. Alternatively a self-normalization method uses ray-sums of coincidences from the emission scan to correct for block pile-up effects [13].

In addition to within-block effects, the detector of the High Resolution Research Tomograph (HRRT) [14] has an additional dimension of the pile-up effect, due to the phoswich system used to determine the depth of interaction (DOI). At high count rates, events are mispositioned from the front to back layer (see below). Thus, a comprehensive correction for pulse pile-up within a CBN is highly desirable.

In this work, we develop and implement a CBN technique for the HRRT. In this technique, embedded in a list mode reconstruction algorithm, the efficiency factors are adjusted ac-

Manuscript received October 6, 2006; revised February 1, 2007. This work was supported in part by the Intramural Research Program of the NIH, NIMH, Warren Grant Magnuson Clinical Center, and Center for Information Technology.

M. Rodriguez, S. Chelikani, T. Mulnix, and R. E. Carson are with the PET Center, Yale University School of Medicine, Yale University, New Haven, CT 06536-0805 USA (e-mail: richard.e.carson@yale.edu)

J.-S. Liow is with the Molecular Imaging Branch, National Institute of Mental Health, National Institutes of Health, Bethesda, MD 20892-9634 USA.

S. Thada and W. C. Barker are with the PET Department, Warren Grant Magnuson Clinical Center, National Institutes of Health, Bethesda, MD 20892 USA.

M. Sibomana and C. Michel are with the Molecular Imaging Division, Siemens Medical Solutions, Knoxville, TN 37932 USA.

C. A. Johnson is with the Division of Computational Bioscience, Center for Information Technology, National Institutes of Health, Bethesda, MD 20892 USA.

Digital Object Identifier 10.1109/TNS.2007.897824

0018-9499/$25.00 © 2007 IEEE

cording to the measured (instantaneous) singles rate in the reconstructed object to account for pile-up effects. Therefore, this technique introduces a new way to correct for pile-up effects in the HRRT as part of the image reconstruction process. One should, however, note that the proposed methodology is also applicable for estimating normalization factors in sinogram reconstruction mode.

II. Background

A. The HRRT

The HRRT [14] is a 3D brain-dedicated scanner. It has 8 detector panels, each consisting of 117 detector blocks (9 in-plane $\times$ 13 axial). Each block has 128 detectors, in an array composed of 2 layers. Each crystal measures 2.1 mm $\times$ 2.1 mm $\times$ 10 mm (transaxial $\times$ axial $\times$ depth). Crystal identification on each panel is performed with a quadrant-sharing photomultiplier (PMT) design, where an array of 10×14 PMTs is centered on the corners of a 9×13 grid of blocks. The double crystal layer LSO/LYSO design serves the purpose of measuring DOI [15]. This measurement is based on sampling the integrated light output at two times, 60 and 180 ns [16], and calculating the early: late ratio. Since the scintillators have different signal decay constants, the ratio identifies the crystal of interaction, with higher ratio values assigned to LSO, due to its faster light output.

The HRRT has a total of 119808 crystals which produce a total of 4.5×10^9 potential LORs, since each detector panel is in coincidence with the 5 opposite panels. With the goal of resolution recovery, we have developed a list-mode reconstruction algorithm (MOLAR, see below) in which there is no compression (i.e., axial rebinning) of LORs, so normalization information for all 4.5×10^9 LORs is required. Direct or LOR-based normalization techniques require very long data acquisition times in order to have acceptable counting statistics per LOR. Even when data are sorted into (parallel projection) sinograms with axial rebinning (typically span 9, maximum ring difference 67), which compresses the data by a factor of 27.5, the acquisition time for a direct normalization is between 30 and 60 hours.

Thus, a CBN technique is essential. If CBN depends only on knowledge of individual crystal efficiencies, this method will reduce the problem to estimating only 119808 values instead of measuring normalization coefficients for 4.5×10^9 LORs.

B. List Mode Reconstruction—MOLAR

In order to fully exploit the HRRT resolution capabilities we designed and implemented MOLAR, **M**otion compensation **O**SEM **L**ist mode **A**lgorithm for **R**esolution recovery, implemented on a computer cluster [17], [18]. MOLAR preserves the Poisson nature of the measured data, so the algorithm does not include any data precorrection. Assuming the image is reconstructed into a three dimensional grid of J voxels, the expected value of the counts Y_i on LOR i is:

$$E(Y_i) = T\left(\sum_{j=1}^{J} c_{ij} A_i L_i N_i \lambda_j + R_i + S_i\right) \qquad (1)$$

where T is the frame duration, λ_j is the activity of voxel j, c_{ij} is the system matrix (including resolution effects and solid angle correction), A_i is the LOR attenuation coefficient, L_i is the correction for livetime (based on block singles rates) and decay, N_i is the LOR normalization factor, R_i is the estimate of random coincidence rate and S_i is the estimate of scatter coincidence rate. The system matrix term incorporates externally-acquired motion information to correctly determine the voxels that contribute to the LOR. Note that LORs are not rebinned so the estimates of normalization and randoms are based on the original detector pair. The random coincidence rate is calculated from the singles rate and the coincidence timing window width [19]. The scatter contribution is estimated using the single scatter simulation model [20] where the scatter estimate includes normalization (N_i) corrected for differences in photon energy and incident angle. Attenuation is calculated from forward projection of a measured transmission image, reconstructed with MAPTR (with spatial smoothness and intensity priors) [21].

In list mode, only LORs with measured events are processed, so the list mode EM equation [17], [22]–[25] for a frame with I measured events is:

$$\lambda_j^{n+1} = \frac{\lambda_j^n}{TQ_j} \sum_{i=1}^{I} \frac{c_{ij} A_i N_i L_i}{\sum_{j'} c_{ij'} A_i N_i L_i \lambda_{j'}^n + R_i + S_i} \qquad (2)$$

where Q_j is the sensitivity image. The calculation of the sensitivity image ideally requires processing all possible LORs, which in the HRRT case is computationally impractical [17]. We use a random subsampling of the LORs in order to efficiently compute Q_j[17], [26], [27]. The MOLAR algorithm computes the sensitivity image for each image reconstruction. This approach allows the algorithm to easily mask out events from any subset of detectors because the LORs defined by those detectors are also discarded when the sensitivity image is calculated [26]. This capability can even mask an entire layer, which will prove useful in the evaluation of the count-rate dependent normalization. Another advantage of computing the sensitivity image for each reconstruction is the ability to easily account for motion effects in each reconstructed frame.

MOLAR also can simulate list mode acquisitions by using the forward projection model (1) to compute the expected value for a user-defined number of LORs and then generate Poisson realizations. Due to the very large number of LORs, even a high-count frame (e.g., 200 M events) has an average expected value per LOR of $\sim$0.05, so, in this case, Poisson realizations are implemented with binomial sampling. Note that the simulations do not provide information about the physics involved in data collection and image generation; however they are useful to perform algorithm characterization.

Reconstructions with (2) are performed with OSEM [28] implemented on a computer cluster [18]. Events are assigned to subsets based on time, not LOR, i.e., in a modulo fashion based on the order of arrival.

III. Methods

A. Image Reconstruction

All image reconstructions in this work were performed with MOLAR using 2 iterations and 30 subsets. The image size is

$256 \times 256 \times 207$ voxels, each voxel being 1.2 mm $\times$ 1.2 mm $\times$ 1.2 mm. The sensitivity image was computed with a random sub-sampling of 1×10^8 LORs. While reconstruction of real data included modeling of random and scatter coincidences, simulations did not include these effects in order to focus on the impact of inaccuracies in the normalization.

B. Normalization With a Rotating Rod Source

In this component-based normalization method for the HRRT [29], the normalization factor for a given LOR i is given by:

$$N_i = C\varepsilon_{1,i}\varepsilon_{2,i}g_{\mathrm{t}}(\phi_{1,i})g_{\mathrm{a}}(\theta_i)g_{\mathrm{t}}(\phi_{2,i})g_{\mathrm{a}}(\theta_i). \quad (3)$$

C is a leading scale factor to convert count rate to Bq/mL, obtained from phantom measurements. The subscripts 1 and 2 identify the two crystals that define LOR i. The ε factors represent the crystal intrinsic efficiencies to be determined by the normalization process. The factors g_{t} and g_a are the geometric transaxial and axial correction factors which are based on the transaxial (ϕ) and axial (θ) LOR incident angles (with respect to the detector face) and correct for variations in the probability of photon detection. Because of the octagonal panel design of the HRRT, θ values are identical for the two crystals of each LOR, while ϕ values may differ. They are computed analytically as the probability that a photon will be stopped by a known intersection length x of the crystal, accounting for interference by other crystals. The geometrical factors are normalized so that the value is 1.0 for LORs entering the crystal perpendicular to the face.

We use a model for the normalization rotating rod source to develop equations relating the efficiency values to the measured normalization data. Inserting (3) into (1) and assuming no scatter, the measured counts y'_i for the normalization acquisition at LOR i corrected for random coincidences with measured delays becomes:

$$y'_i = \frac{CA_i\varepsilon_{1,i}\varepsilon_{2,i}g_{\mathrm{t}}(\phi_{1,i})g_{\mathrm{a}}(\theta_i)g_{\mathrm{t}}(\phi_{2,i})g_{\mathrm{a}}(\theta_i)\Omega_i d_i}{\cos\theta_i} \quad (4)$$

where Ω_i is the coincidence solid angle correction (calculated from the inverse of the sum of the squared distances from the source to each detector position, assuming a Gaussian point spread function). The total activity intersected by LOR i is calculated as the ratio of d_i (the in-plane length of intersection of LOR i with the normalization source model) and the term $\cos\theta_i$, which corrects for the increased intersection length of axially oblique LORs. For the rotating line, the source model is an annulus, with inner and outer radii of 15 and 16 cm, respectively. Note that dead time and decay correction are incorporated into the leading constant term C in (4) under the assumption that these factors are approximately constant for all LORs, for each acquisition. Rearranging (4) and solving for the ε factors to be determined, yields:

$$\varepsilon_{1,i}\varepsilon_{2,i} = \frac{y'_i\cos\theta_i}{CA_i g_{\mathrm{t}}(\phi_{1,i})g_{\mathrm{a}}(\theta_i)g_{\mathrm{t}}(\phi_{2,i})g_{\mathrm{a}}(\theta_i)\Omega_i d_i}. \quad (5)$$

We developed an iterative algorithm to estimate ε values. Consider a specific crystal k and the set of LORs I_k where k is one of the two crystals of the LOR and which intersect the normalization source. Summing both sides of (5) over all LORs in I_k yields [30]:

$$\varepsilon_k = \frac{\sum_{i\in I_k}\frac{y'_i\cos\theta_i}{CA_i g_{\mathrm{t}}(\phi_{1,i})g_{\mathrm{a}}(\theta_i)g_{\mathrm{t}}(\phi_{2,i})g_{\mathrm{a}}(\theta_i)\Omega_i d_i}}{\sum_{i\in I_k}\varepsilon_{2,i}}. \quad (6)$$

The derivation was performed in this manner to permit calculation of the list-mode data-dependent terms in the numerator once. An alternative form which produces the maximum likelihood estimate [31] is more computationally demanding since these terms enter the denominator, multiplied by ε^n, and thus must be recalculated at each iteration. To improve convergence, the following iterative expression to update the crystal efficiencies ε_k was derived:

$$\varepsilon_k^{n+1} = \beta\varepsilon_k^n + (1-\beta)\frac{\sum_{i\in I_k}\frac{y'_i\cos\theta_i}{CA_i g_{\mathrm{t}}(\phi_{1,i})g_{\mathrm{a}}(\theta_i)g_{\mathrm{t}}(\phi_{2,i})g_{\mathrm{a}}(\theta_i)\Omega_i d_i}}{\sum_{i\in I_k}\varepsilon_{2,i}^n} \quad (7)$$

where n represents the iteration number and β is an optional damping term $(0 \le \beta < 1)$ used to facilitate convergence. At convergence $(\varepsilon^{n+1} = \varepsilon^n)$, (6) is satisfied. In the iterative process, all efficiencies were initialized to 1.0 and the final efficiency values were normalized so that the mean value is 1.0. For data from the rotating source, ten iterations were required for the computed efficiencies to converge to within 0.1 % of their final value.

In order to assess the noise in the computed efficiency values, a 2-h scan was acquired with the rotating rod source ($\sim$20 MBq). Five replicates of efficiency values were computed using 3, 6, 12 and 24 min of list-mode data. The coefficient of variation of ε values across the replicates was computed in order to assess the statistical variability of the crystal efficiencies as a function of the total counts in the normalization acquisition.

C. Efficiency Variation With Activity

In the previous section, we described a method to measure the crystal efficiencies at a specific count rate. Based on pulse pile-up considerations, crystal efficiencies will change with count rate so that when the normalization count rate is different from the count rate of an emitting object, artifacts may appear in the reconstructed images. Therefore, this apparent efficiency variation with activity level was measured. For this purpose, crystal efficiencies at different mean block singles rates (S) were computed. The normalization source in this case was a 20-cm diameter cylinder filled with ^{18}F centered in the field of view. While a cylindrical phantom is not generally considered to be an ideal source for normalization measurements due to scatter, it was an appropriate choice to assess the count rate dependence in ε (see Section V).

The procedure was as follows:

— Acquire 13 20-min emission scans with a delay of 10 min between acquisitions. Ideally each emission scan should be acquired at a constant activity, but a 20-min acquisition time was chosen in order to have good statistics at the low activity acquisitions. The total number of prompts in the

first frame was 1600×10^6 and in the last frame was 160×10^6.

— Compute the efficiencies for crystal k from each acquired emission file j ($\varepsilon_{k,j}$) using (7), including the same solid angle correction, so that efficiency values were computed for each crystal at different measured block singles rate values (S_j). For the uniform phantom, the factor d_i was calculated as the intersection length of LOR i and the 20-cm cylinder. Only LORs intersecting the transverse central 10 cm of the cylinder were used in order to reduce sensitivity to small errors in this source model when approaching the edge of the phantom. Fast monotonic convergence with data from the uniform phantom was achieved with a damping term β of 0.5; oscillating slow convergence was seen with $\beta = 0$. Other β values (0.2, 0.4, 0.6) showed convergence to the same efficiency estimates, albeit at different speeds.

— The 13 ε values for each crystal were fitted to a linear model ($\varepsilon_{k,j} = \alpha_k S_j + b_k$) in order to obtain a value of the slope α for each crystal k. For S_j, the measured singles rate at the block containing crystal k was used. Note that since the mean ε value over all crystals is 1, the mean α_k value over all crystals is $\sim$0.

— During subsequent image reconstructions, the crystal efficiencies obtained with the normalization rod source (ε_k) are adjusted according to the instantaneous block singles rate S and the fitting parameter α as:

$$\varepsilon'_k = \varepsilon_k + \alpha_k(S - S_0) \tag{8}$$

where S_0 is the average block singles rate during the rotating source normalization ($\sim$4000 cps in this work). Note that crystal efficiency adjustment could also be implemented by storing b_k rather than ε_k, which avoids the need to store S_0.

Thus, in the proposed method, the base efficiency values ε_k are determined from the rotating source, but the count-rate dependent adjustments are based on the decaying uniform phantom. As will be seen in Section IV, α values were positive in the back layer (LYSO) and negative in the front layer (LSO).

D. Efficiency Adjustment With Singles Rate

To assess the importance of the count-rate dependent efficiency correction, simulated and real data were obtained to evaluate the impact of the efficiency adjustment proposed in (8). Simulations were carried out with the forward projection model of the reconstruction algorithm (1). Effects unrelated to normalization specifically, scatter and random coincidences and live-time effects, were not included. A 20-cm uniform phantom was simulated using the modeled crystal efficiencies, predicted with (8). Specifically, ε' values were computed using the estimated ε and α values from the HRRT, extrapolated to a high singles rate ($S = 30$ K cps, corresponding to $\sim$145 MBq in the scanner field-of-view), with $S_0 = 4000$ cps. Approximately 800×10^6 events were simulated. For the measured data, we acquired a 10-min scan of a 20-cm uniform phantom at high activity levels ($\sim$145 MBq), with $\sim 600 \times 10^6$ prompt coincidences, and estimated randoms and scatter fractions of 36 and 41%, respectively. This acquisition had a noise-equivalent count (NEC) of $\sim 100 \times 10^6$ events. We reconstructed these list mode files using 4 different count-rate dependencies of the efficiency values, as follows:

a) *None*. No adjusting parameters, i.e., $\alpha_k = 0$ for all crystals.

b) *Layer*. The α_k values were averaged over panel, block and crystal; therefore we adjusted the efficiency for all crystals with one common α value (positive for the back layer, and negative for the front layer).

c) *Block*. All the α_k values were averaged over panel and block, resulting in 128 α values.

d) *Individual*. An individual adjusting parameter for each crystal, therefore 119808 α values were used.

The reconstructed images of simulated data were evaluated visually to detect artifacts. In addition, the reconstructed (mean of a centered cylindrical ROI, 7 cm in-plane radius and 12 cm axially) and true values (20 KBq/ml) were compared. To further assess the artifact pattern, radial profiles of the reconstructed images were obtained for both simulated and real data with the origin at the center of the gantry field-of-view. The reconstructed values were binned into radial segments of 2 mm and the average within each bin was computed. The number of voxels per bin varied from 1200 (center) to 72400 (at 6 cm). The profile variability with radius was assessed for the 4 correction methods listed above.

E. Front/Back Layer Reconstructions

As described above, MOLAR allows masking of events detected at determined group of detectors. Since the HRRT has two crystal layers, a way to further validate the normalization method is to reconstruct the same object with events only from either the back layer or the front layer, as if there were two different scanners. This evaluation was motivated by the difference in singles rate dependencies found for front and back layers. If all corrections are accurate, the reconstructions should be equivalent to each other, excluding statistical differences. Note that there is a factor of $\sim$10 difference in statistics between front-front and back-back coincidence events.

A 3-h decaying ^{11}C uniform 20-cm phantom scan was acquired and 25 frames were reconstructed using the efficiency values obtained from the rotating source with and without adjustment according to the singles rate. Separate reconstructions were performed using either events from the front layer (front-front coincidences) or the back layer (back-back coincidences). For both front and back layers, two sets of reconstructions were performed using the methods named *None* and *Layer* (see Section III.D for details). The mean value of a large centered cylindrical ROI (in-plane $\mathrm{radius} = 7$ cm and axial $\mathrm{length} = 12$ cm) was computed and plotted against the average block singles rate.

IV. Results

A. Normalization With a Rotating Rod Source

Based on a 2-hour acquisition of a rotating rod source of $\sim$17 MBq, the mean estimated values of ε for the front and back layer

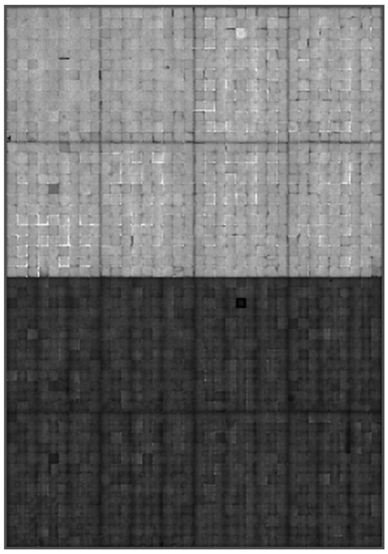

Fig. 1. Crystal efficiencies computed from the normalization rod source data and the iterative algorithm (7). The top two rows represent the front layer (LSO) and the bottom two rows, the back layer (LYSO). The first and third rows show detector panels 0–3 and the second and fourth rows show detector panels 4–7. Each panel contains a grid of 9 (horizontal) by 13 (vertical) blocks.

were 1.52 ± 0.19 and 0.48 ± 0.11, respectively, i.e., an efficiency ratio of $\sim 3:1$. This ratio is consistent with the linear attenuation coefficients of LSO (.086 mm^{-1}) and LYSO (.053 mm^{-1}) and the detector depth (10 mm). Fig. 1 shows an illustration of the efficiency values. The detector blocks are easily visualized since the efficiency values are lower at the edge crystals of the block. Edge crystals of the panels have particularly low efficiency. Within a block, the average efficiency of the edge crystals is 1.49 ± 0.26 and at the center is 1.55 ± 0.08 for the front layer; for the back layer, these values are 0.46 ± 0.13 and 0.54 ± 0.07, respectively. The relatively larger range of efficiency in the back layer is partially caused by the organization of the photomultipliers and their analog electronics, grouped by 3 in transverse direction, which introduces vertical stripes in ε's.

Replicate efficiency computations for scan durations of 3, 6, 12, and 24 min were performed with average number of counts (n_1) of 67, 133, 267, and 533×10^6 events. The coefficients of variation in percent across the replicates for the front layer were 2.8, 1.9, 1.4, 1.0, and for the back layer, 5.4, 3.8, 2.7, 1.9, respectively. As expected, the coefficient of variation decreased with $\sqrt{n_1}$ and the front layer showed less variability due to higher counting statistics. A lower bound on the coefficient of variation of the ε values can be computed from the average number of coincident counts per crystal (n_2) under Poisson assumptions, i.e., $1/\sqrt{n_2}$. The average number of counts per crystal for the 4 different times was 1.8, 3.5, 7.0 and 14.0×10^3 for the front layer. For the back layer, the numbers were 0.5, 1.0, 1.9 and 3.8×10^3. For example, for the front-layer shortest scan, the lowest possible coefficient of variation is 2.4 % compared to the measured value of 2.8%. Thus, the mathematical form of the algorithm for ε estimation (7) introduces at most a moderate statistical penalty.

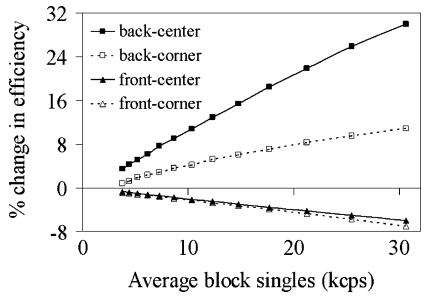

Fig. 2. Average efficiency variation with block singles rate at the corner and center of block detectors. This variation is computed as the percent change with respect to the extrapolated value at $S = 0$.

B. Efficiency Variation With Activity

The variation of the estimated efficiency values with singles rate, computed from the 13 decaying ^{18}F emission scans is illustrated in Fig. 2. The estimated ε values were averaged in 4 groups (the center 4 crystals per block and the corner 4 crystals per block, in both front and back layers), and are plotted versus average block singles rates (S) as the percent difference with respect to the extrapolated value at $S = 0$.

This figure shows two effects:

1) *Between-layer*. The efficiency of crystals in the front layer (triangle symbol) decreases and the efficiency of crystals in the back layer (square symbol) increases with activity. This variation is linear for both layers. Linear fits to the four datasets had r^2 coefficients ranging from 0.984 to 0.999.
2) *Within-layer*. Events from the corner crystals (dashed lines) are pushed to the center of the block (solid lines) at higher singles rates. This effect is more clearly seen in the back layer data since within-layer pile-up is often accompanied by between-layer pile-up.

The knowledge that the efficiency changes linearly with the measured singles rate motivated the proposal for the adjustment of crystal efficiencies computed from the rotating rod source, as expressed in (8). Over the 119808 crystals, mean $(\pm\text{SD})$ α values were $-3.2 \times 10^{-6} \pm 2.1 \times 10^{-6}$ and $+3.3 \times 10^{-6} \pm 1.6 \times 10^{-6}$ for the front and back layers, respectively. The linear fit of the slope value, α, had an average standard error (the uncertainty of the slope estimate determined by the fit) of $\sim 25\%$ for the front layer and 15% for the back layer, suggesting that the large variability in estimated α across crystals is not due solely to statistical noise in the data. We found no correlation between the crystal efficiencies (from the rotating source) and α values; this supports the mathematical form of the efficiency adjustment model (8), since both terms are independent.

The analysis of α values provides additional information. When examining α at average panel level (Fig. 3), it can be seen that the magnitude of between-layer pile-up is smaller for blocks on the edge of the panel, presumably due to quadrant-sharing PMT design (see Section V).

C. Efficiency Adjustment With Singles Rate

As mentioned above (Section III.D), four types of adjustment to crystal efficiencies in simulated and real data were evaluated.

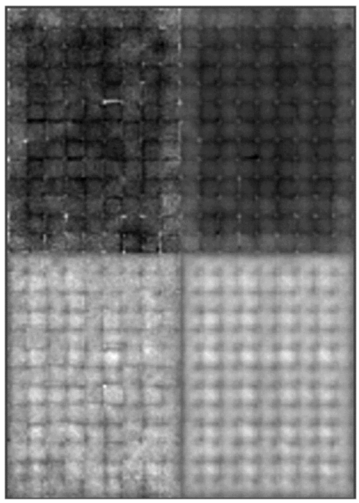

Fig. 3. Illustration of estimated α values. The first column shows the α values per crystal for a typical detector panel. The second column shows the α value per crystal, averaged over the 8 panels. The top row corresponds to the front (LSO) layer and the bottom row is the back (LYSO) layer. Images are displayed on a scale of -8.0 to +8.0 ($\times 10^{-6}$).

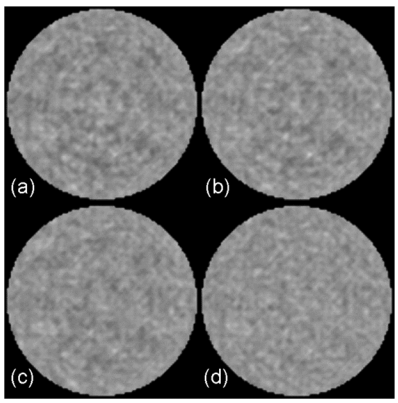

Fig. 4. Images reconstructed from the simulated acquisition of a 20-cm uniform cylinder, comparing reconstructions implementing the four efficiency adjustments with the count rate: (a) None, (b) Layer, (c), Block, and (d) Individual (see Section III.D for details). The images shown here are the central in-plane 12 cm of the reconstructed phantom, averaged over the central axial 12 cm (100 slices) and displayed on a scale of 60–125% of the mean.

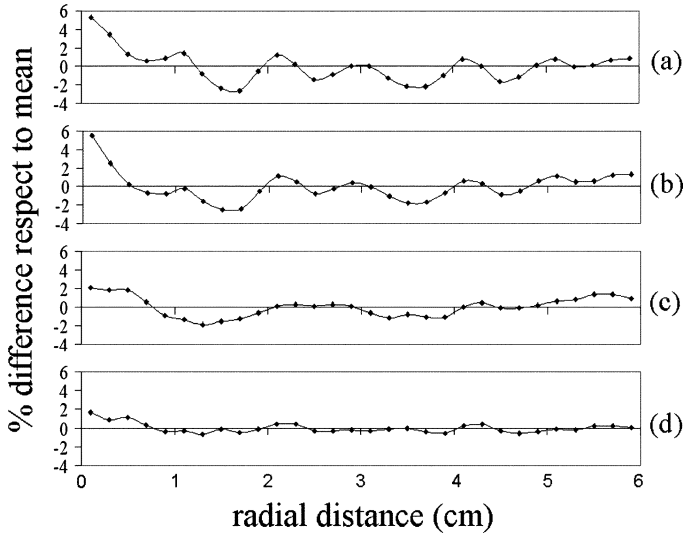

Fig. 5. Percent difference of the reconstructed activity values within radial bins with respect to the mean activity in the central 6 cm radius the simulated 20 cm uniform phantom. Profiles are shown for reconstructions implementing the four efficiency adjustments with the count rate: (a) None, (b) Layer, (c), Block, and (d) Individual (see Section III.D for details).

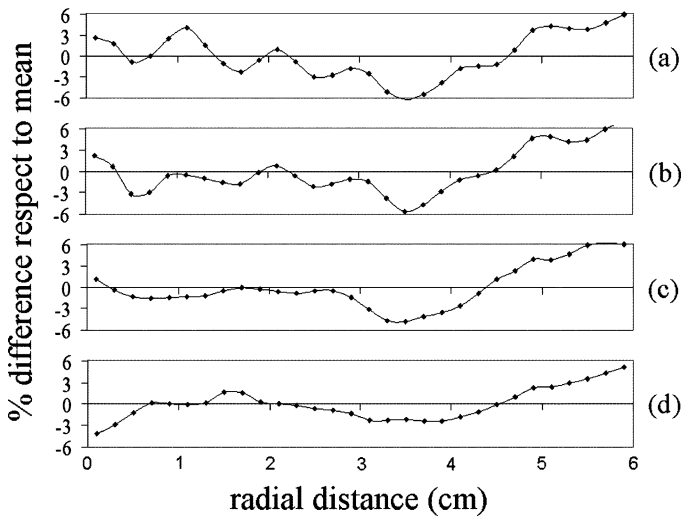

Fig. 6. Percent difference of the reconstructed activity value within radial bins with respect to the mean activity value in the central 6-cm radius for the measured 20-cm cylinder uniform phantom. Profiles are shown for reconstructions implementing the four efficiency adjustments with the count rate: (a) None, (b) Layer, (c) Block, and (d) Individual (see Section III.D for details).

In the case of simulated data, the mean reconstructed activity with the four efficiency adjustment methods listed above had a percent bias of -1, -0.3, -0.5 and 0.2%. This confirms that errors in normalization factors do not tend to produce global, low-frequency errors, but are more likely to produce high-frequency effects.

Fig. 4 shows a comparison of the reconstructed images using these four efficiency adjustment methods for simulated data. This figure shows the average of the reconstructed activity over the 100 central slices. Only the middle 12 cm in-plane is shown for better visualization of the artifact. Without efficiency adjustment, there are circular/octagonal artifacts present in the reconstructed image. The efficiency adjustment with only one α value does not solve the problem because this correction primarily addresses layer differences, not pile-up effects between crystals at different positions in the block. Visually, efficiency adjustment methods c and d (128 and 119808 α values) produce very similar images without the artifact. The same behavior was found in the reconstructed images of real data, although the artifact visible in Fig. 4(a) and (b) was not easily displayed, perhaps due to the lower NEC than in the simulated data.

Fig. 5 shows the reconstructed activity plotted against the distance from the center of the images shown in the Fig. 4. There is a clear oscillating pattern if the full correction is not performed. The percent coefficients of variation of the reconstructed values for the four efficiency adjustments across the 2 mm-bins were: 1.7, 1.6, 1.1 and 0.5, respectively.

Fig. 6 illustrates the same comparison as in Fig. 5 but for the reconstructions of real phantom data. Clearly in these images,

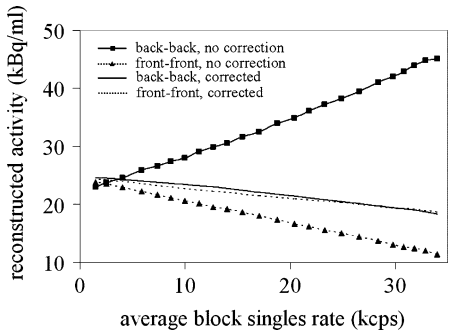

Fig. 7. Mean of the reconstructed images using only events from front-front or back-back coincidences. The lines with symbols (squares for back-back events and triangles for front-front events) represent reconstructions without count rate correction for crystal efficiencies. The lines without symbols (solid line for back-back events and dashed line for front-front events) represent reconstructions with count rate correction for crystal efficiencies. The correction applied was the *layer* efficiency adjustment (see Section III.D for details). Decay correction, but not livetime correction, has been applied.

there are other factors that affect uniformity beyond the accuracy of the efficiency adjustment, so that the advantages of using 119808 α values are less obvious from the radial profiles. However, as with the simulation data, the oscillatory patterns seen in Fig. 6(a) and (b) are eliminated in (c) and (d). The profile for Fig. 6(d) is more uniform than the rest. The percent coefficients of variation of activity values across the 2 mm-bins in Fig. 6 were: 3.3, 3.2, 3.1 and 2.2 for methods a through d, respectively.

D. Front/Back Layer Reconstructions

The dependence of the reconstructed activity on phantom activity is shown in Fig. 7 for reconstructions of front layer coincidences or back layer coincidences. These data are corrected for decay and not corrected for detector livetime. Ideally, curves for reconstructed activity from front-front and back-back coincidences would lie on top of each other. However, without adjusting the crystal efficiency with singles rate (lines with symbols, Fig. 7), diverging behavior is observed, with the reconstructed activity with back layer events increasing with count rate because events detected in the front layer are mispositioned into the back layer due to pile-up effects at high count rates (see Section V).

Due to the count-rate dependent efficiency changes (Fig. 2), a change in reconstructed activity of $\sim$ the square of the change in crystal efficiency would be expected. However, the magnitude of this effect is larger; this is attributed to the underestimation of randoms which are calculated from the block singles and the uncorrected crystal efficiencies [19]. When the simplest efficiency adjustments studied in this work (*Layer* method) is implemented in these reconstructions, the two curves overlap (lines without symbols, Fig. 7) almost exactly, suggesting that the new method corrects for the layer mispositioning effects.

V. Discussion

In this work, we implemented a component-based normalization for the HRRT. This is a very important step, particularly for list-mode reconstruction, due to the very large number of LORs. In addition, this normalization method has been extended to address pile-up effects. Various hardware and software approaches have been proposed to address this effect in the past. We have extended these approaches with a method which uses a continuous linear model within the image reconstruction procedure. This is especially useful when reconstructing dynamic studies with list-mode reconstruction where this correction can be made using the instantaneous singles rate. This is also the first approach where pile-up effects are measured for individual crystals as part of the routine normalization procedure.

1) Component-Based Normalization: Several component-based normalization methods have been proposed for PET which are different than the method proposed here in terms of the components included in the normalization (3). For example, we did not include the time alignment component described in [6]. Time alignment techniques have been developed for the HRRT so that the timing adjustments that can be made as part of the detector tuning process are on the order of a few hundred picoseconds [32] which is negligible compared to the timing window of 6 nsec. Therefore, we believe that the impact of time alignment factors will be minor.

The geometrical factors g in (3) can be computed analytically or directly estimated from phantom measurements. Techniques to measure the g factors have been proposed using a variety of sources for geometric transaxial and axial correction [6], [33]. In this work, they are computed from the linear attenuation probabilities in the crystal, which clearly is an oversimplification. Errors in the g factors would most likely produce low resolution inhomogeneities in the reconstructed images. Two approaches could be taken to improve the accuracy of the g factors. First, Monte Carlo simulations of crystal interactions could be performed [34]. Alternatively, with knowledge of the ε values, a similar derivation to that performed from (4)–(7) could be used to develop an iterative algorithm to estimate the g factors. Taken further, a generalization of (7) would allow for both crystal efficiencies and geometric factors to be computed iteratively from the same dataset [31].

The data acquisition time for our CBN method depends on the variability we wish to achieve in crystal efficiency values. In this work, the goal was an average statistical noise of $\sim$1% for which $\sim$50 min is required at the current source activity, extrapolating from the 1.0% and 1.9% variability of the 24-min replicates for front and back layers, respectively. It is interesting to determine how precise the normalization values should be. Consider a dynamic study with good total statistics, i.e., $\sim$4 billion events. Therefore, for list-mode reconstruction, we would expect $\sim$1 event per LOR. Since a Poisson count with a mean of 1 has 100% standard deviation, 1% uncertainty in the efficiency factors should clearly be more than sufficient. Therefore, it is likely that a normalization acquisition of much less than one hour will produce only minor increases in variability in reconstructed images.

2) Comparison With LOR-Based Normalization: It would be natural to expect to compare the results of a component-based method to a direct LOR-based method; however, this comparison is not feasible. In this work, efficiencies are computed with statistical variability of $\sim$1%, so that each normalization factor for an LOR has a variability of $\sim$2%. Even if 10% variability was acceptable, 100 events/LOR are needed in order to have

10% statistical variability, thus requiring $\sim 4.5 \times 10^{11}$ events. The activity of the source at the time of these measurements provided approximately 1×10^9 events/h. Therefore the LOR based technique would require an acquisition of 450 hours or $\sim$20 days.

3) Source of Pile-Up: In the HRRT, pulse pile-up produces two effects: pushing events from the corner to the center of each block (*within-layer* pile-up) and from the front layer to the back layer (*between-layer* pile-up). As seen in Fig. 2, *within-layer* pile-up is more clearly observed in the back layer because events pushed from the front layer are simultaneously being pushed to the center of the block, in other words, a combination of *within-layer* and *between-layer* pile-up. *Within-layer* pile-up has been described previously [9], [11]. The magnitude of this type of pile-up is likely to be smaller on the HRRT than previous-generation scanners due to the smaller block size and the PMT quadrant sharing technology. When pile-up occurs in a quadrant sharing approach [35], events do not necessarily move towards the block center, except when pile-up occurs in the same physical block.

Between-layer pile-up is a result of the HRRT logic for measuring DOI [15]. Layer discrimination is based on the ratio of two measurements of the output signal of the PMTs from the LSO/LYSO phoswich. Our hypothesis is that the summed signal from two quickly rising front-layer events, arriving at different times during the pulse integration period, is interpreted as a single slowly rising back-layer event. Consequently, the two events in the front layer will be incorrectly placed as one event in the back layer. The probability of this occurrence increases with the activity in the object.

4) Count-Rate Dependence: The main difference between our method and other CBN methods is the ability to measure how the crystal efficiencies change with activity using (8). An alternative approach is that of self-normalization [13] whereby block profile factors are determined using ray-sums of emission sinogram data. We chose to not follow this approach because 1) the large axial field-of-view (FOV) of the HRRT introduces substantial variations in block singles rates, so pile-up effects vary regionally, and 2) our correction is applied on an event-by-event basis from list mode, so our method does not require pre-binning of event data.

The efficiency adjustment developed here corrects in the image reconstruction process for the *apparent* sensitivity changes caused by pile-up effects. Clearly, there are no true count-rate dependent changes in efficiency, since the apparent variations are due to photon mispositioning. The adjustment scheme where individual α values are applied to adjust the efficiency of each crystal produces the best results in terms of image quality and variability. For the front layer, α shows a coefficient of variation of 66% and for the back layer the variability is 49%. Part of this variability is within the block clearly due to crystal position (Fig. 2). However, the average coefficient of variation of α at the same block position is 62% and 45% in front and back layers, respectively, suggesting that there are other factors contributing to between-block differences in pile-up.

An analysis of α at the panel level gives additional insights into the pile-up effect (Fig. 3). The magnitude of pile-up depends upon the total crystal volume that detects single events and contributes light which can corrupt signal integration. In the PMT quadrant sharing approach, this crystal volume varies with position in the panel. For example, the four PMTs coupled to a central block are also sensitive to events in the neighboring 8 blocks. On the edge of a panel, there are only 5 neighboring blocks contributing to pile-up (3 for the corner blocks). This explains the α pattern seen in Fig. 3. This effect is expected to be corrected by using the efficiency adjustment method *d (Individual)*, while method *c* (*Block*) will fail to account for pile-up differences between blocks.

Measuring α can be made part of the routine normalization measurement since it is possible that this parameter will change together with the crystal efficiency. As we do not currently have sufficient longitudinal data on the stability of α, it would be prudent to acquire such data over time in order to determine if routine α measurement is necessary.

5) Applicability to Sinogram-Based Normalization: The proposed methodology is also applicable when list-mode data are sorted into sinograms (with compression/axial rebinning). The normalization data are processed, as described above, to produce ε and α values. The sinogram-mode normalization correction is then calculated by inverting a sinogram built from the product of those crystal efficiencies (corrected for frame-average singles rate per block) for all relevant LORs, including the geometry factors (g_{t}, g_{a} and Ω). With a uniform ^{68}Ge calibration phantom scan binned into sinograms, a one-hour CBN produced reconstructed images of better quality than those produced with a 60-hour direct normalization using the same rotating rod source acquisition (data not shown).

6) Rod Sources and Uniform Phantoms: In this method, the crystal efficiencies are determined using a rotating rod source and the parameters to adjust them for count-rate dependence are determined from a 20-cm uniform cylinder. A more straightforward approach might be to perform normalization scans with two (or more) rotating rod sources of different strengths. However, it is important to recognize that pile-up is produced by photons with a range of energies, wider than those accepted by the scanner energy windows. For example, a line source will have very few scattered photons, so the measured singles in the energy window will be an accurate measure of the rate of singles that can produce pile-up. As object size increases, the fraction of scattered photons increases, so that there will be more low energy events striking the crystals and causing pile-up, but not being measured as part of the singles rate. In other words, it is likely that the magnitude of event mispositioning at a measured singles rate S with the rotating rod source will be comparable to the event mispositioning caused at a lower *measured* singles rate for the 20-cm uniform cylinder. Thus in the case of the HRRT targeted for human brain imaging, accurate measurement of α should be performed with an object with similar scatter properties to the human head, e.g., a 16–20 cm diameter phantom. Note, however, that it is likely that an accurate method to measure α could be performed with other geometries, such as multiple rods of different strength, so long as an appropriate correction for low-energy photon contributions is made.

Our method requires the definition of the reference normalization singles rate S_0 (8). This situation presents a challenge

since the measured singles rate during the normalization scan is not the appropriate value, as described above. One possible approach to determine the S_0 value is to use the images reconstructed with either front-front or back-back coincidences (Fig. 7). The crossing point between these reconstructed activity lines should correspond to the activity where no correction to the rod source ε values is necessary, i.e., the intersection may define the appropriate S_0 in (8). Note in Fig. 7 that this intersection corresponds to $\sim$2500 cps which is lower than the singles rate derived from the rotating source measurements (4000 cps).

The efficiency values estimated from the 20-cm cylinder and the ones obtained from the rotating source were compared by computing the difference and following its in-plane behavior. The efficiencies from the rotating source were 2% lower at the edges of the detector panels and 2% higher in the center of the panel. This difference is attributed to the presence of scatter in the cylinder source which we did not include in the normalization model (d_i in (4)). Therefore, we would expect that the α values at the edges and the center will have the estimated errors of -2 and $+2\%$, respectively.

7) Choice of Normalization Source Geometry: One aspect of the rotating rod as a source for efficiency calculations is that the crystal efficiencies are not measured at a constant singles rate since the crystal-source distance is continuously changing during the normalization data acquisition. With a source of $\sim$16 MBq, on average, the block singles rate changes from 2000 to 6000 cps as the source rotates around the gantry opening. This represents an efficiency variation during the normalization data acquisition of $\sim$1% and 3% for the front and back layer, respectively (Fig. 2). This variation would be higher for a higher activity source. One approach to reduce this rotational variation is by using a smaller rotation radius for the source. Note that this approach is not applicable to direct normalization since it truncates the tomographic FOV.

Due to scatter, a 20-cm uniform cylinder is not considered to be an ideal source to compute the efficiency values to be used in a component-based normalization, since these values are used to define LOR efficiency for unscattered photon pairs. The rotating source produces $\sim$10% scattered coincidences (based on sinogram analysis) so a natural question that arises from this work is why not use a small cylindrical source (with minimal scatter) for the calculation of both ε and α values. A centered cylindrical source has the advantage of an unchanging singles rate during the normalization data acquisition. In addition, it is likely that human heads will have more similar solid angle effects to a centered cylinder than a rod source rotating on the edge of the field-of-view. We evaluated this option using a smaller cylinder (5-cm diameter) and we found that satisfactory results can be obtained for measurement of ε. However, as the object gets smaller, the precise definition of the source geometry becomes critical [36]. Positioning errors on the order of 1 mm in the location of the small cylinder in the ε calculation produced clearly visible artifacts in reconstructed images.

8) Effect of Pile-Up on Spatial Resolution: Pulse pile-up degrades reconstructed spatial resolution [9]. The MOLAR algorithm provides great flexibility in terms of the selection of different resolution models for each LOR [17], [37] based on factors such as crystal layer and incident angle. Thus, a logical next step is to incorporate pile-up information into the resolution model and to assess whether reconstructed resolution is unaffected by count rate and pile-up effects.

VI. Conclusion

In this work, we have implemented a component-based normalization technique for the HRRT that accounts for crystal efficiency variations with count rate due to pile-up effects. The method has two parts. First, the crystal efficiencies are computed from data acquired from the rotating source with an average statistical error of $\sim$1% from an acquisition of $<$1 hour. Second, the count rate dependency of the crystal efficiencies is measured with a 20-cm decaying uniform phantom and efficiencies are adjusted according to the count rate with a linear model. In the initial evaluation, this method eliminated pile-up-induced reconstruction artifacts at high count rates.

References

[1] E. J. Hoffman, T. M. Guerrero, G. Germano, W. M. Digby, and M. Dahlbom, "PET system calibrations and corrections for quantitative and spatially accurate images," *IEEE Trans. Nucl. Sci.*, vol. 36, no. 1, pp. 1108–1112, Feb. 1989.

[2] M. Defrise, D. W. Townsend, D. Bailey, A. Geissbuhler, C. Michel, and T. Jones, "A normalization technique for 3D PET data," *Phys. Med. Biol.*, vol. 36, pp. 939–952, 1991.

[3] J. S. Liow and S. C. Strother, "Normalization using rotating rods for 3D PET," in *Proc. 3rd Int. Meeting Fully Three-Dimensional Image Reconstruction in Radiology and Nuclear Medicine*, Aix-les-Bains, France, 1995, pp. 61–65.

[4] M. E. Casey, H. Gadagkar, and D. Newport, "A component based method for normalization in volume PET," in *3rd Int. Meeting Fully Three-Dimensional Image Reconstruction in Radiology and Nuclear Medicine*, Aix-les-Bains, France, 1995, pp. 67–71.

[5] R. D. Badawi, M. A. Lodge, and P. K. Marsden, "Algorithms for calculating detector efficiency normalization coefficients for true coincidences in 3D PET," *Phys. Med. Biol.*, vol. 43, pp. 189–205, 1998.

[6] R. D. Badawi and P. K. Marsden, "Developments in component-based normalization for 3D PET," *Phys. Med. Biol.*, vol. 44, pp. 571–594, 1999.

[7] B. Bai, Q. Li, C. H. Holdsworth, E. Asma, Y. C. Tai, A. Chatziioannou, and R. M. Leahy, "Model-based normalization for iterative 3D PET image reconstruction," *Phys. Med. Biol.*, vol. 47, pp. 2773–2784, 2002.

[8] M. Conti, J. Hamill, and W. K. Luk, "Component-based normalization for panel detector PET scanners," *IEEE Trans. Nucl. Sci.*, vol. 51, no. 1, pp. 16–20, Feb. 2004.

[9] G. Germano and E. J. Hoffman, "A study of data loss and mispositioning due to pileup in 2D detectors in PET," *IEEE Trans. Nucl. Sci.*, vol. 37, no. 2, pp. 671–675, Apr. 1990.

[10] J. S. Karp, G. Muehllehner, D. Beerbohm, and D. Mankoff, "Event localization in a continuous scintillation detector using digital processing," *IEEE Trans. Nucl. Sci.*, vol. 33, no. 1, pp. 550–555, Feb. 1986.

[11] W.-H. Wong and H. Li, "A scintillation detector signal processing technique with active pileup prevention for extending scintillation count rates," *IEEE Trans. Nucl. Sci.*, vol. 45, no. 3, pp. 838–842, Jun. 1998.

[12] H. Li, W.-H. Wong, J. Uribe, H. Baghaei, Y. Liu, Y. Wang, T. Xing, and M. Aykac, "A new pileup-prevention front-end electronic design for high resolution PET and gamma cameras," *IEEE Trans. Nucl. Sci.*, vol. 49, no. 5, pp. 2051–2056, Oct. 2002.

[13] R. D. Badawi and P. K. Marsden, "Self-normalization of emission data in 3D PET," *IEEE Trans. Nucl. Sci.*, vol. 46, no. 3, pp. 709–712, Jun. 1999.

[14] K. Wienhard, M. Schmand, M. E. Casey, K. Baker, J. Bao, L. Eriksson, W. F. Jones, C. Knoess, M. Lenox, M. Lercher, P. Luk, C. Michel, J. H. Reed, N. Richerzhagen, J. Treffert, S. Vollmar, J. W. Young, W. D. Heiss, and R. Nutt, "The ECAT HRRT: Performance and first clinical application of the new high resolution research tomograph," *IEEE Trans. Nucl. Sci.*, vol. 49, no. 1, pp. 104–110, Feb. 2002.

[15] J. W. Young, J. C. Moyers, and M. Lenox, "FPGA based front-end electronics for a high resolution PET scanner," *IEEE Trans. Nucl. Sci.*, vol. 47, no. 4, pp. 1676–1680, Aug. 2000.

[16] C. Knoess, "Evaluation and optimization of the High Resolution Research Tomograph," Ph.D. dissertation, Aachen, Germany, 2004, ISBN 3-8322-3337-7.

[17] R. E. Carson, W. C. Barker, J.-S. Liow, S. Adler, and C. A. Johnson, "Design of a motion-compensation OSEM list-mode algorithm for resolution-recovery reconstruction of the HRRT," in *Proc. IEEE Nuclear Science Symp.*, Portland, OR, 2003, pp. 3281–3285.

[18] C. A. Johnson, S. Thada, Y. Zhao, A. Iano-Fletcher, J.-S. Liow, W. C. Barker, R. L. Martino, and R. E. Carson, "Software architecture of the MOLAR-HRRT reconstruction engine," in *Proc. IEEE Nuclear Science Symp.*, Rome, Italy, 2004, pp. 3956–3960.

[19] W. C. Barker, J.-S. Liow, Y. Zhao, S. Thada, A. Iano-Fletcher, M. Lenox, C. Michel, C. A. Johnson, and R. E. Carson, "Randoms estimation for list-mode reconstruction for the ECAT HRRT," in *Proc. IEEE Nuclear Science Symp.*, Rome, Italy, 2004, pp. 3510–3513.

[20] C. C. Watson, "New, faster image-based scatter correction for 3D PET," *IEEE Trans. Nucl. Sci.*, vol. 47, no. 4, pp. 1587–1594, Aug. 2000.

[21] J. Nuyts, P. Dupont, S. Stroobants, A. Maes, L. Mortelmans, and P. Suetens, "Evaluation of maximum-likelihood based attenuation correction in positron emission tomography," *IEEE Trans. Nucl. Sci.*, vol. 46, no. 4, pp. 1136–1141, Aug. 1999.

[22] L. Parra and H. H. Barrett, "List-mode likelihood: EM algorithm and image quality estimation demonstrated on 2-D PET," *IEEE Trans. Med. Imag.*, vol. 17, pp. 228–235, 1998.

[23] R. Levkovitz, D. Falikman, M. Zibulevsky, A. Ben-Tal, and A. Nemirovski, "The design and implementation of COSEM, an iterative algorithm for fully 3-D listmode data," *IEEE Trans. Med. Imag.*, vol. 20, pp. 633–642, 2001.

[24] J. Qi, G. J. Klein, and R. H. Huesman, "Image properties of list-mode likelihood reconstruction for a rectangular positron emission mammograph with DOI measurements," *IEEE Trans. Nucl. Sci.*, vol. 48, no. 4, pp. 1343–1349, Aug. 2001.

[25] A. Rahmim, M. Lenox, A. J. Reader, C. Michel, Z. Burbar, T. J. Ruth, and V. Sossi, "Statistical list-mode image reconstruction for the high resolution research tomograph," *Phys. Med. Biol.*, vol. 49, pp. 4239–4258, 2004.

[26] M. Rodriguez, W. C. Barker, S. Thada, J.-S. Liow, A. Iano-Fletcher, C. A. Johnson, and R. E. Carson, "Characteristics of list mode reconstruction for the HRRT," *J. Nucl. Med.*, vol. 46, p. 56P, 2005.

[27] J. Qi, "Calculation of the sensitivity image in list-mode reconstruction," *IEEE Trans. Nucl. Sci.*, vol. 53, no. 5, pp. 2746–2751, Oct. 2006.

[28] H. M. Hudson and R. S. Larkin, "Accelerated image reconstruction using ordered subsets of projection data," *IEEE Trans. Med. Imag.*, vol. 13, pp. 601–609, 1994.

[29] J.-S. Liow, M. Chen, W. C. Barker, Y. Zhao, S. Thada, A. Iano-Fletcher, M. Lenox, C. Michel, R. B. Innis, C. A. Johnson, and R. E. Carson, "Component-based normalization for the ECAT-HRRT," *J. Nucl. Med.*, vol. 46, p. 166P, 2005.

[30] N. C. Ferreira, R. Trebossen, C. Comtat, M. C. Gregoire, and B. Bendriem, "Iterative crystal efficiency calculation in fully 3-D PET," *IEEE Trans. Med. Imag.*, vol. 19, pp. 485–492, 2000.

[31] D. Hogg, K. Thielemans, T. Spinks, and N. Spyrou, "Maximum likelihood estimation of normalisation factors for PET," in *Proc. IEEE Nuclear Science Symp. Conf. Rec.*, San Diego, CA, 2001, pp. 2065–2069.

[32] M. W. Lenox, Z. Burbar, J. Young, T. Gremillion, and C. Knoess, "Coincidence time alignment of high resolution planar detectors," in *Proc. IEEE Nuclear Science Symp.*, Norfolk, VA, 2002, pp. 956–959.

[33] D. L. Bailey, D. W. Townsend, P. E. Kinahan, S. Grootoonk, and T. Jones, "An investigation of factors affecting detector and geometric correction in normalization of 3D PET data," *IEEE Trans. Nucl. Sci.*, vol. 43, no. 6, pp. 3300–3307, Dec. 1996.

[34] S. Jan *et al.*, "GATE: A simulation toolkit for PET and SPECT," *Phys. Med. Biol.*, vol. 49, pp. 4543–4561, 2004.

[35] W. H. Wong, J. Uribe, K. Hicks, and M. Zambelli, "A 2-dimensional detector decoding study on BGO arrays with quadrant sharing photomultipliers," *IEEE Trans. Nucl. Sci.*, vol. 41, no. 4, pp. 1453–1457, Aug. 1994.

[36] M. Rodriguez, W. C. Barker, J. S. Liow, S. Thada, S. Chelikani, T. Mulnix, and R. E. Carson, "Count rate dependent component-based normalization for the HRRT," *J. Nucl. Med.*, vol. 47, p. 197P, 2006.

[37] R. Yao, V. Rathod, C. Jose, S. Thada, C. A. Johnson, and R. E. Carson, "Point spread function (PSF) determination for use in HRRT listmode reconstruction," *J. Nucl. Med.*, vol. 46, p. 169P, 2005.